

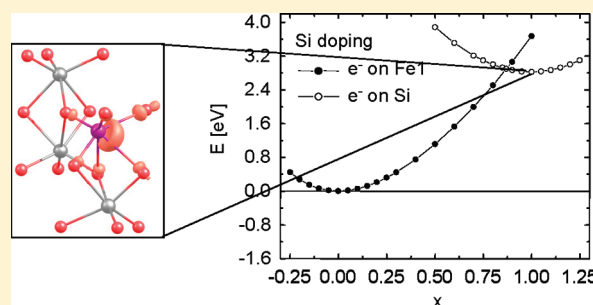
# Electron Transport in Pure and Doped Hematite

Peilin Liao,<sup>†</sup> Maytal Caspary Toroker,<sup>‡</sup> and Emily A. Carter<sup>\*,†,§</sup>

<sup>†</sup>Departments of Chemistry and <sup>‡</sup>Mechanical and Aerospace Engineering, Program in Applied and Computational Mathematics, and <sup>§</sup>Gerhard R. Andlinger Center for Energy and the Environment, Princeton University, Princeton, New Jersey 08544-5263, United States

**ABSTRACT:** Hematite ( $\alpha\text{-Fe}_2\text{O}_3$ ) is a promising candidate for photoelectrochemical splitting of water. However, its intrinsically poor conductivity is a major drawback. Doping hematite to make it either p-type or n-type enhances its measured conductivity. We use quantum mechanics to understand how titanium, zirconium, silicon, or germanium n-type doping affects the electron transport mechanism in hematite. Our results suggest that zirconium, silicon, or germanium doping is superior to titanium doping because the former dopants do not act as electron trapping sites due to the higher instability of Zr(III) compared to Ti(III) and the more covalent interactions between silicon (germanium) and oxygen. This suggests that use of n-type dopants that easily ionize completely or promote covalent bonds to oxygen can provide more charge carriers while not inhibiting transport.

**KEYWORDS:** Iron oxides, electron transport, n-type doping



Utilization of solar energy is proposed to be an important means to satisfy the increasing global energy demand.<sup>1</sup>  $\alpha\text{-Fe}_2\text{O}_3$  (“ $\alpha$ ” is omitted henceforth) has attracted interest from researchers due to its optimal optical band gap (2.0–2.2 eV, capable of absorbing  $\sim 40\%$  of the solar spectrum),<sup>2</sup> low cost, abundance, nontoxicity, and stability. On the basis of its valence band and conduction band alignments with respect to water redox potentials, pure hematite is capable of oxidizing water to generate oxygen, but can only reduce water to form hydrogen with an applied electrical bias.<sup>3</sup> However, Hu et al.<sup>4</sup> recently demonstrated that a  $\text{CoF}_3$  solution used to modify a Ti-doped hematite surface can shift the conduction band position such that an external bias is not required to reduce water to hydrogen, suggesting full water splitting to hydrogen and oxygen may be achieved with doped hematite. A state-of-the-art hematite photoanode, reported by Tilley et al.,<sup>5</sup> achieved a water oxidation photocurrent of  $>3 \text{ mA}/\text{cm}^2$  using nanostructured hematite with an  $\text{IrO}_2$  cocatalyst at an applied potential of +1.23 V versus the reversible hydrogen electrode under standard solar illumination conditions.

Low conductivity is one of the major factors limiting the use of hematite in solar energy conversion applications. Other factors include a low optical absorption coefficient (due to an indirect band gap) and a high electron–hole recombination rate.<sup>6–8</sup> Nanotexturing and use of nanorods to improve light trapping may overcome the former, while doping to increase carrier concentrations may overwhelm the latter, as discussed below. Electron mobility in hematite at room temperature is of the order of  $10^{-2} \text{ cm}^2/\text{V}\cdot\text{s}$ ,<sup>9,10</sup> compared to  $1350 \text{ cm}^2/\text{V}\cdot\text{s}$  for silicon.<sup>11</sup> The measured activation energy  $E_a$  for hematite conductivity, which accounts for both carrier formation and hopping mobility, varies nonmonotonically with temperature; for  $T > 800^\circ\text{C}$ ,  $E_a$  is  $\sim 1.0 \text{ eV}$ ; for  $450^\circ\text{C} < T < 800^\circ\text{C}$ , the presence of defects or

impurities decreases  $E_a$  to a value of  $\sim 0.1 \text{ eV}$ ; below  $450^\circ\text{C}$ ,  $E_a$  is  $\sim 0.7 \text{ eV}$ , influenced by grain boundary or surface effects.<sup>12,13</sup> For nonconcentrated solar energy applications, the lower temperature range is most relevant.

Doping affects conductivity through changing carrier concentrations and/or carrier mobility.  $\text{Fe}_2\text{O}_3$  is usually referred to as an n-type semiconductor due to naturally occurring oxygen vacancies in the bulk. It can be made either p-type through Mg doping,<sup>9,14</sup> or n-type through Ti, Zr, Si, or Ge doping,<sup>15–19</sup> with conductivity significantly increased (by orders of magnitude) in both cases. Photoelectrochemical activity of hematite is also improved with Ti, Zr, Si, or Ge doping.<sup>17,19–22</sup> The measured solubility limit for Si (Ge) in  $\text{Fe}_2\text{O}_3$  is  $\sim 2$  (2.5) atomic percent (at. %, defined as  $x/2$  for dopant M in a chemical composition of  $\text{Fe}_{2-x}\text{M}_x\text{O}_3$ ),<sup>23</sup> while Zr doping up to 10.0 at. % has been achieved without forming a new phase<sup>19</sup> and Ti can be continuously added to substitute for Fe until ilmenite ( $\text{FeTiO}_3$ ) is formed.<sup>24</sup> Such high doping levels can have a profound effect on the conductivity of the host material. Although dopants might also occupy interstitial sites or segregate to grain boundaries, here we focus on cation substitution at lattice sites, since this site occupancy has been used to explain various experiments.<sup>19,25,26</sup> Moreover, later we show that these large cation dopants greatly prefer to occupy substitutional rather than interstitial sites. Their site occupancy at grain boundaries is not considered here, and so our results are most directly comparable to single crystal samples.

In this Letter, we use ab initio quantum mechanics calculations to gain insight at the atomic scale as to how n-type doping with Ti, Zr, Si, or Ge affects electron transport in  $\text{Fe}_2\text{O}_3$ . Although

**Received:** January 30, 2011

**Revised:** March 15, 2011

**Published:** March 22, 2011

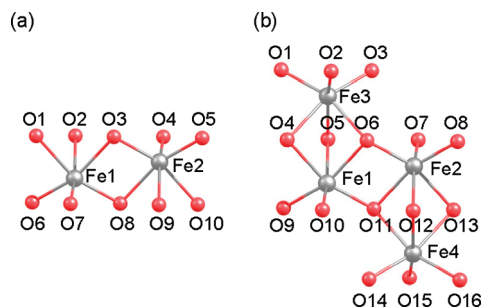


**Figure 1.** Cluster models used in this work: (a)  $\text{Fe}_2\text{O}_{10}^{15-}$  and (b)  $\text{Fe}_4\text{O}_{16}^{21-}$ . The capping ECPs and point charge arrays are not shown. Fe ions are in gray. O ions are in red. This color scheme is followed throughout.

transport properties of doped hematite have not been studied theoretically before, Rosso et al.<sup>27</sup> and Iordanova et al.<sup>28</sup> used quantum chemical cluster calculations to evaluate the transport properties of pure hematite within the small polaron model that we adopt here. We follow their approach with one modification: we adopt an electrostatically embedded cluster model described below (see Figure 1 for illustration) whereas they employed a covalent embedding procedure in which the dangling bonds on oxygen atoms on the edges of their clusters were saturated by hydrogen atoms. We chose instead to use a large point charge array, converged with respect to size, to mimic the long-range electrostatic effects from the bulk surroundings that are likely to be important in ionic crystals such as hematite.<sup>29</sup> We first outline the theory used to evaluate carrier transport and then provide computational details, followed by results and discussion, and finally the conclusions.

Electron transport in hematite can be understood within the small polaron model<sup>30</sup> in which the movement of charge carriers is coupled to distortions of nearby atoms and the charge carrier hops (transfers) from site to site. To apply the small polaron model, we first optimize the local crystal structure for the electron carrier localizing on the initial (labeled as “A”) or final (labeled as “B”) site for the electron transfer. A linear nuclear reaction coordinate<sup>31</sup> is then used to calculate two potential energy (PE) curves

$$q_x = (1 - x)q_A + xq_B \quad (1)$$

where  $q_A$  ( $q_B$ ) are collective nuclear coordinates of the optimized crystal structure when the electron is localized on site A (B), and  $x$  determines the fraction along the nuclear reaction coordinate (see Figure 2 as an example). The two PE curves are termed “diabatic” in this paper, since the added electron remains on the same site as the nuclear coordinates are changed along each PE curve, implying small derivative couplings between electronic states.<sup>32</sup> The diabatic activation energy  $\Delta G^*$  is the energy difference between the crossing point of the two curves and the corresponding minimum.  $\Delta G^*$  is smaller than the overall activation energy  $E_a$  for conductivity, because  $E_a$  also includes the energy required to form a mobile hole/electron.<sup>33</sup> However,  $\Delta G^*$  is an upper bound on the electron transfer activation barrier, since the adiabatic barrier will be lower by the magnitude of the coupling matrix element. The reorganization energy  $\lambda$  is the energy difference between  $x = 0$  and  $x = 1$  of the acceptor PE curve (see Figure 2 for illustration). Detailed discussion of the model can be found in the paper by Farazdel et al.<sup>31</sup> Here our

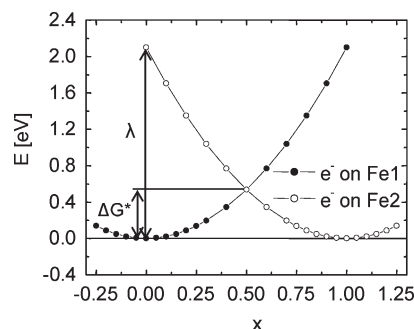


**Figure 2.** UHF potential energy curves along the nuclear reaction coordinate for electron transfer between Fe1 and Fe2 in the  $\text{Fe}_4\text{O}_{16}^{21-}$  cluster. The empty and full circles represent actual calculation data points. The energy for  $x = 0$  on the left curve is set to zero.

focus is on trends in the diabatic activation energy, as the mobility of carriers depends exponentially on its value

$$\mu \propto e^{-\Delta G^*/kT} \quad (2)$$

where  $\mu$  is the electron mobility,  $T$  is the temperature, and  $k$  is the Boltzmann constant. The electron conductivity can be calculated from the electron mobility using the equation

$$\sigma = en\mu \quad (3)$$

where  $\sigma$  is the electron conductivity,  $e$  is the electron charge, and  $n$  is the electron carrier concentration.

Two clusters  $\text{Fe}_2\text{O}_{10}^{15-}$  and  $\text{Fe}_4\text{O}_{16}^{21-}$  are used in our simulations (see Figure 1). Capping aluminum effective core potentials (ECPs)<sup>34</sup> are used to replace Fe(III) cations that would have been bonded to the terminating oxygen anions. Use of such ECPs prevents electron density on the oxygen anions from artificially drifting outward, by providing effective Pauli repulsion at nearest neighbor cation sites. Al ECPs are used because they have similar ionic radii to Fe(III) cations. The clusters with capping ECPs are then embedded in a large point charge array meant to represent the extended ionic crystal, where charges of +3 and −2 represent Fe and O ions in the bulk, respectively, and the charges of ions on the edges or surfaces are determined through Evjen’s method.<sup>35</sup> The clusters and point charge arrays are built from the experimental crystal structure.<sup>36</sup> The experimental antiferromagnetic ordering of bulk hematite is maintained in the clusters: irons labeled Fe1 and Fe2 in Figure 1a, b have parallel spin, but their spins are antiparallel to those of Fe3 and Fe4 in Figure 1b. Because of the antiferromagnetic ordering and the (3d)<sup>5</sup> high-spin configuration of Fe(III) cations, a (forbidden) spin flip would be required for transfer to Fe cations in adjacent layers. Therefore, the added electron can only transfer between Fe cations within the same layer (Fe1 and Fe2 in Figure 1). Transport between Fe adjacent layers in pure  $\text{Fe}_2\text{O}_3$  was observed experimentally<sup>37,38</sup> to make an insignificant contribution to the mobility; the theoretical work of Iordanova et al. confirmed this finding.<sup>28</sup>

The cluster in Figure 1b is used to study dopant effects. Two different dopant substitutions are explored: substitution of Fe2, simulating electron transfer between Fe and the dopant; or substitution of Fe4, modeling electron transfer between Fe cations with one of them closer to the dopant. These two models provide an estimate of the maximum effect that dopants impose on electron mobility through cation substitutions at lattice sites.

Since Si (Ge) is usually tetrahedrally coordinated in the solid state, it is important to determine its site preference within the hematite lattice where the cations are all octahedrally coordinated. In earlier work, we showed that density functional theory+U (DFT+U)<sup>39–41</sup> with the PBE<sup>42</sup> generalized gradient approximation (GGA) exchange–correlation functional and an ab initio-derived value of  $U - J = 4.3$  eV for Fe(III) describes hematite very well.<sup>43</sup> Thus, we ran a full geometry optimization at the level of periodic PBE+U ( $U - J = 4.3$ ) theory for a 30-atom hexagonal unit cell of  $\text{Fe}_2\text{O}_3$  with one Fe vacancy and one Si (Ge) dopant. The cell with Si (Ge) residing in the Fe site as a substitutional dopant (6-fold coordinated) is lower in energy by at least 0.56 (1.72) eV per 30 atoms compared to the cell with Si (Ge) in the tetrahedral site, because there are significant lattice distortions induced by tetrahedrally coordinated Si (Ge). There are two symmetry-unique tetrahedral sites in this hexagonal unit cell; this octahedral-tetrahedral energy difference quote above is for the lowest energy tetrahedral site, which is closest to the vacancy. We regard these energy differences as lower bounds on the energy of placing a Si (Ge) atom in a tetrahedral site in a perfect hematite lattice with no Fe vacancy present, since the vacancy provides a place to relieve lattice strain. From these data, we conclude that Si or Ge as dopants in hematite prefer to substitute for Fe rather than reside in interstitial sites.

Hay–Wadt basis sets (contracted as 3s3p2d) and ECPs are used for Fe, Ti, and Zr with only the 1s, 2s, and 2p electrons subsumed within the ECPs for Fe and Ti and the 1s, 2s, 2p, 3s, 3p, and 3d electrons described by the ECP for Zr.<sup>44</sup> A Stuttgart basis set augmented with diffuse and polarization functions from the Pople-type 6-31+G\* is used for O, with 1s electrons subsumed into the ECP.<sup>45,46</sup> A 6-31+G\* (6-311G\*) all-electron basis is used for Si (Ge).<sup>47,48</sup> This choice of basis sets converges the activation energy to <0.1 eV compared to larger basis sets. The point charge array adopted consists of a  $3 \times 3 \times 3$  supercell of the hexagonal representation of hematite (a total of 954 point charges), which converges the activation energy to <0.03 eV compared to a  $5 \times 5 \times 3$  supercell (a total of 2514 point charges).

Geometry optimizations are performed at the unrestricted Hartree–Fock (UHF) level; all atoms are allowed to relax in the field of the fixed capping ECPs and point charges until the maximum force component on any atoms is below 0.023 eV/Å. Since UHF theory does not account for any electron correlation, complete active space self-consistent field (CASSCF) theory is also employed to explore the significance of static correlation. CASSCF calculations were performed on the UHF-optimized structure of the  $\text{Fe}_2\text{O}_{10}^{15-}$  cluster in Figure 1a with an active space of 11 Fe 3d electrons in 10 Fe 3d orbitals. Adding O 2p electrons to the active space does not affect the activation energy calculated, implying the size of the active space is sufficient. DFT is not employed here because of its problems with describing both charge transfer and open-shell transition metal systems due to its tendency toward self-interaction and delocalization errors.<sup>49</sup> The NWChem program<sup>50</sup> is used for all UHF calculations. CASSCF calculations are performed with the GAMESS package.<sup>51</sup>

**Electron Transport in Pure Hematite.** We first consider the transfer of an added electron between the Fe(III) cations denoted as Fe1 and Fe2 in both clusters (see Figure 1). The additional electron represents one that was, for example, photoexcited to the conduction band elsewhere in the crystal and is now moving through the crystal. For the  $\text{Fe}_2\text{O}_{10}^{15-}$  cluster, UHF and CASSCF theories predict nearly identical PE curves along

**Table 1. Diabatic Activation Energy  $\Delta G^*$  (eV) and Reorganization Energy  $\lambda$  (eV) for Pure Hematite, As Calculated Using Electrostatically-Embedded Cluster Models Described by Unrestricted Hartree–Fock (UHF) and Complete Active Space Self-Consistent Field (CASSCF) Theories<sup>a</sup>**

	$\text{Fe}_2\text{O}_{10}^{15-}$		$\text{Fe}_4\text{O}_{16}^{21-}$
	UHF	CASSCF	UHF
$\Delta G^*$	0.50	0.50	0.53
$\lambda$	1.97	1.98	2.07

<sup>a</sup> The overall embedded cluster models have charge of  $-1$  (via capping ECPs and point charge arrays; see text for details).

the nuclear reaction coordinate for electron transfer, with  $\Delta G^*$  and  $\lambda$  (see Table 1) being  $\sim 0.5$  and  $\sim 2.0$  eV, respectively, implying that contributions from static correlation to  $\Delta G^*$  or  $\lambda$  are small. Therefore, reliable results can be obtained for the  $\text{Fe}_4\text{O}_{16}^{21-}$  cluster (Figure 1b) using only UHF theory, which will be used to model both pure and doped hematite. Figure 2 displays the UHF PE curves along the nuclear reaction coordinate for electron transfer in the  $\text{Fe}_4\text{O}_{16}^{21-}$  cluster. Each PE curve exhibits harmonic behavior and the two PE curves are symmetric with respect to  $x = 0.5$  for pure hematite. The overlap integral between the donor and acceptor wave functions at  $x = 0.5$  is 0.070 for the electrostatically embedded  $\text{Fe}_4\text{O}_{16}^{21-}$  cluster, which is close to 0.066 reported by Rosso et al.<sup>27</sup> for a similar cluster capped with H atoms. The small overlap confirms the localized character of the electron carrier within the donor and acceptor wave functions. Increasing the cluster size to  $\text{Fe}_4\text{O}_{16}^{21-}$  increases  $\Delta G^*$  and  $\lambda$  by only 0.03 and 0.10 eV, respectively (Table 1). The Fe–O bond lengths in the two clusters at  $x = 1$  with the added electron on the Fe2 site differ by 0.05 Å at most. The small energy and geometry differences indicate that the electron transfer process for hematite localizes around the Fe donor and Fe acceptor sites and therefore is well characterized by the smaller cluster.

Experimental and theoretical activation energies have been reported previously. Morin<sup>52</sup> and Goodenough<sup>53</sup> estimated an activation energy of 0.1 eV for hematite from mobility measurements, which accounts for hopping mobility alone, in contrast to  $E_a$  discussed in the introduction. Rosso et al.<sup>27</sup> obtained a diabatic activation energy  $\Delta G^* = 0.25$  eV using clusters capped with H atoms. They used a crystal geometry optimized by periodic DFT–GGA to build their clusters and then fixed certain angles during geometry optimization, while our values use geometries optimized with the electrostatically embedded cluster scheme starting from experimental crystal structures. Given the highly ionic nature of hematite, we believe that our structures are derived from a more physically correct description of the crystal. Although Rosso et al.<sup>27</sup> obtained adiabatic values in good agreement with experiment ( $\sim 0.1$  eV), we find that the electron coupling matrix element (needed to estimate the adiabatic barrier) calculated within the NWChem code<sup>50</sup> is highly sensitive to the accuracy of the wave function overlap integral. We therefore eschew calculating adiabatic barriers and only report the rigorous upper bounds provided by the diabatic barriers. Our reported values are larger than Morin and Goodenough’s estimates, as they should be since they are upper bounds. However, given the 0.4 eV discrepancy between the experimental estimate and our prediction, we focus on qualitative trends rather than quantitative predictions in what follows.



**Table 2.** UHF Diabatic Activation Energies  $\Delta G^*$  (eV) and Reorganization Energies  $\lambda$  (eV) for Ti-, Zr-, Si-, or Ge-doped  $\text{Fe}_4\text{O}_{16}^{21-}$  Electrostatically Embedded Clusters<sup>a</sup>

dopant M		M substitutes for Fe2		M substitutes for Fe4	
		Fe2 $\rightarrow$ M	M $\rightarrow$ Fe2	Fe1 $\rightarrow$ Fe2	Fe2 $\rightarrow$ Fe1
Ti	$\Delta G^*$	0.07	1.56	0.42	0.67
	$\lambda$	2.24	2.15	2.11	2.13
Zr	$\Delta G^*$	2.21	0.01	0.30	0.86
	$\lambda$	-	1.94	2.16	2.14
Si	$\Delta G^*$	2.90	0.07	0.49	0.57
	$\lambda$	-	3.67	2.09	2.12
Ge	$\Delta G^*$	2.32	0.07	0.42	0.65
	$\lambda$	-	3.15	2.08	2.11

<sup>a</sup> $\lambda$  is not available for “-” since the solution converged to the lower energy state where the electron is localized on the iron atom rather than the dopant. See Figure 1 for locations of Fe1, Fe2, and Fe4 atoms.

**Electron Transport in n-Doped Hematite.** Table 2 summarizes the calculated electron transfer parameters when hematite is n-doped. In all these cases, the magnitudes of the overlap integrals between the donor and acceptor wave functions at the crossing point geometry of the PE curves are less than 0.1, suggesting localization of the electron carrier within the donor or acceptor states.

We first analyze the effect of Ti doping. For electron transfer between Fe and Ti, the state with the electron localized on the Ti site is lower in energy by  $\sim 1.5$  eV compared to the state with the electron localized on the Fe (Figure 3a). The stabilization effect of the Ti site can be explained as follows.  $\text{Ti}^{4+}$  has completely empty 3d orbitals, and  $\text{Fe}^{3+}$  has five localized 3d electrons. The electron carrier added to the  $\text{Ti}^{4+}$  site does not experience any repulsion from Ti 3d electrons whereas the one added to the  $\text{Fe}^{3+}$  site is repelled by those five Fe 3d electrons present, especially the 3d electron with which it shares an orbital. Therefore, the state with the electron localized on Ti is preferred and is much lower in energy. As a result, due to the exothermicity of the electron transfer from Fe to Ti, the activation energy for transfer from Fe to Ti (0.07 eV) is much smaller than the activation energy required for the electron to exit the Ti site (1.56 eV). For electron transfer between Fe sites in the presence of a nearby Ti, the  $\Delta G^*$ s differ slightly for the two directions but both are close in magnitude (around 0.5 eV) to those for the pure case. As illustrated in Figure 3b, the state with the electron on Fe2 (closer to Ti) is more stable by  $\sim 0.25$  eV than the state with the electron on Fe1 (further away from Ti). The stabilization of the electron on Fe2 is driven by the larger electrostatic attraction of  $\text{Ti}^{4+}$  compared to  $\text{Fe}^{3+}$ .

X-ray photoemission and electron energy loss spectra indicate that  $\text{Fe}^{2+}$  and  $\text{Ti}^{4+}$ , instead of  $\text{Ti}^{3+}$ , is present in samples with Ti concentrations between 6 and 50 at. % (the latter forming ilmenite).<sup>26,53,54</sup> Periodic DFT or DFT+U calculations using unit cells with Ti concentrations of 8.3–50 at. % confirmed these oxidation states,<sup>55–58</sup> though pure DFT is not reliable for hematite.<sup>59</sup> The embedded cluster here models the limit of very low dopant concentrations. Ionization potentials (IPs) of isolated ions derived from optical spectra show that the IP of  $\text{Ti}^{3+}$  to  $\text{Ti}^{4+}$  (43.27 eV) is 12.6 eV larger than the IP of  $\text{Fe}^{2+}$  to  $\text{Fe}^{3+}$  (30.65 eV),<sup>60</sup> suggesting that  $\text{Ti}^{3+}$  is favored over  $\text{Fe}^{2+}$  in the limit of isolated ions. To explore this issue further, we ran

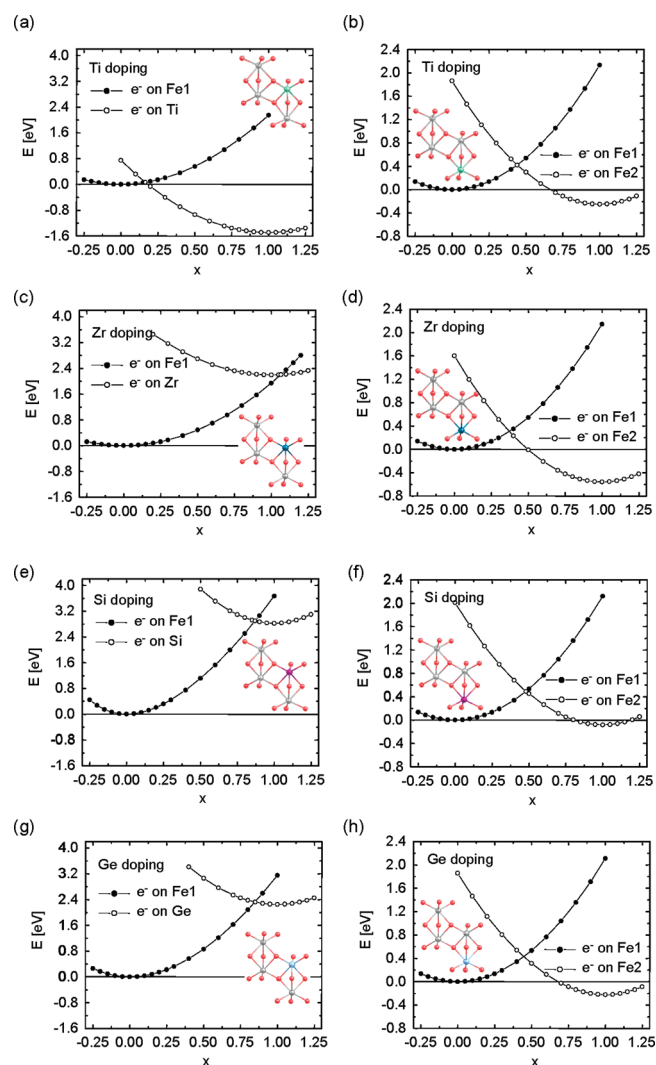


**Figure 3.** UHF potential energy curves along the nuclear reaction coordinates for electron transfer between (a) Fe1 and Ti and (b) Fe1 and Fe2 with Ti doping, between (c) Fe1 and Zr and (d) Fe1 and Fe2 with Zr doping, between (e) Fe1 and Si and (f) Fe1 and Fe2 with Si doping, and between (g) Fe1 and Ge and (h) Fe1 and Fe2 with Ge doping. The hollow and solid circles represent actual calculation data points. The energy for  $x = 0$  on the left curve is set to zero. The figures within the plot show the location of the dopant in the cluster, Ti in green, Zr in dark blue, Si in purple, and Ge in light blue.

periodic PBE+U ( $U - J = 4.3$  eV for both Fe and Ti, so as not to introduce any bias toward localization on either metal) calculations using 30-atom and 120-atom ( $2 \times 2 \times 1$ )  $\text{Fe}_2\text{O}_3$  supercells, both with only one Ti substitution (corresponding to  $\sim 8.3$  and  $\sim 2.1$  at. %, respectively). We found that while the extra electron is of mostly Fe 3d character in the 30-atom cell, it is of mostly Ti 3d character in the 120-atom cell, which further consolidates the results from embedded clusters. Overall, in the low dopant concentration limit, Ti acts as a trapping site for electrons and is therefore clearly not an optimal dopant choice.

Next we proceed to analyze results for Zr doping. For electron transfer between Fe and Zr, Figure 3c shows that the PE curve with the electron on Zr is much higher in energy (the minima of the two PE curves differ by  $\sim 2.2$  eV), suggesting that the electron

**Table 3. Summary of M–O Bond Lengths in Å<sup>a</sup>**

	Fe(III)	Fe(II)	Ti(III)	Zr(III)	Si(III)	Ge(III)
M–O6	2.00	2.16	2.00	2.10	1.69	1.87
M–O7	2.05	2.09	2.10	2.18	2.47	2.25
M–O8	2.04	2.13	2.09	2.19	1.82	1.98
M–O11	2.18	2.34	2.20	2.28	2.55	2.39
M–O12	2.17	2.32	2.16	2.25	1.84	2.07
M–O13	2.15	2.29	2.15	2.24	2.53	2.39

<sup>a</sup> “M” stands for various elements of different oxidation states positioned at “Fe2” as in Figure 1b. O atoms are indexed as in Figure 1b.

carrier always stays on the Fe site, forming Fe<sup>2+</sup> and Zr<sup>4+</sup>, in contrast to the electron transfer between Fe and Ti (Figure 3a). This difference between Zr and Ti is reflected in their IPs. The IP of Zr<sup>3+</sup> is 34.34 eV, which is ~8.9 eV smaller than that of Ti<sup>3+</sup> (43.27 eV).<sup>60</sup> Even though the IP of Zr<sup>3+</sup> is still ~3.6 eV higher than that of Fe<sup>2+</sup> (30.65 eV), the difference is much smaller than that between Ti<sup>3+</sup> and Fe<sup>2+</sup>, and here the crystal field effects of the oxygen ions serve to strongly favor Fe<sup>2+</sup> over Zr<sup>3+</sup> (less metal–ligand repulsion for the small Fe<sup>2+</sup>). The electron transfer between Fe and Fe, with Zr nearby, is similar to that with Ti. The difference between the minima of the two PE curves (~0.56 eV, Figure 3d) is twice as large as that with Ti<sup>4+</sup> (~0.25 eV, Figure 3b), indicating stronger electrostatic attraction from Zr<sup>4+</sup> than Ti<sup>4+</sup>. The activation energy is affected by this difference, favoring electron transfer toward the Fe near Zr. Thus, each Zr atom not only donates one electron to hematite thereby increasing carrier concentration, but the Zr atom also repels the added carrier so that the carrier does not get trapped at the dopant site with transport dominated by Fe to Fe electron transfer. We expect Zr to be a better dopant than Ti in the low dopant concentration regime.

Si or Ge doping produces qualitatively similar effects as Zr doping. The electron carrier strongly prefers to be localized on an Fe site compared to a Si (Ge) site, with the Fe site lower in energy by ~2.8 (~2.2) eV (Figure 3e, g). As a result, electron transport will be via Fe sites rather than via the dopant sites, as in the case of Zr doping above. For transfer between Fe sites, the electron carrier is stabilized by ~0.1 (~0.2) eV on Fe2 when a Si (Ge) is nearby (Figure 3f, h). This electrostatic stabilization effect is similar to that of Ti doping but is smaller, suggesting that Si (Ge) is less ionized compared to Ti, consistent with the fact that, for example, silica (SiO<sub>2</sub>) is much more covalent oxide than titania (TiO<sub>2</sub>). The less ionized character of Si or Ge also suggests that the earlier IP analysis for Ti and Zr might not apply to Si or Ge, consistent with the more covalent nature of their oxides. Overall, like Zr, Si or Ge are much more advantageous dopants for improving hematite conductivity compared to Ti.

We now consider two possible explanations as to why Ti and Si (Ge) behave differently, and why Zr and Si (Ge) perform similarly. The first is a geometric effect. Table 3 summarizes the M–O bond lengths (M is positioned as “Fe2” in Figure 1b) for different metal ion oxidation states. For Fe(III), Fe(II), Ti(III), and Zr(III), the M–O bonds can be divided into two groups of bond lengths differing no more than ~0.2 Å, as in the pure hematite crystal. The bond lengths follow the order of Fe(III)–O ≈ Ti(III)–O < Zr(III)–O < Fe(II)–O, which is in agreement with the magnitude of electrostatic attractions from different oxidation states and ionic radii of the transition metal cations. However, in the presence of an added electron, the Si–O

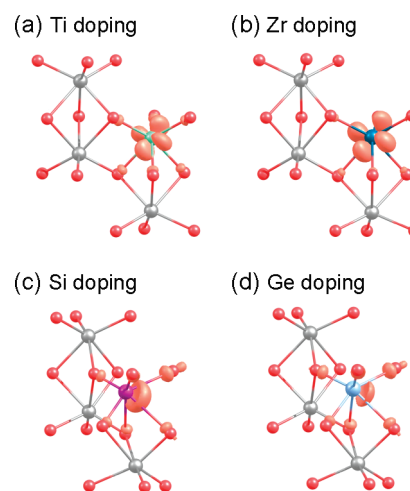


**Figure 4.** Density difference isosurface plots of the added electron localized on the dopant site for (a) Ti doping, (b) Zr doping, (c) Si doping, and (d) Ge doping. The electrostatically embedded cluster for Si or Ge doping is rotated for a clear view. Ti is in green, Zr is in dark blue, Si is in purple, and Ge is in light blue. A contour value of 0.14 electron density/Å<sup>3</sup> is used.

and Ge–O bonds are grouped differently with three of them significantly (up to ~0.8 Å) longer than the others. To decouple electronic from geometric effects, we ran calculations for Ti and Si doping using the geometries optimized for an electron added to pure Fe<sub>4</sub>O<sub>16</sub><sup>21−</sup> at  $x = 0$  and  $x = 1$ , that is, not allowing for further nuclear relaxation upon addition of the dopant. The energy trend of the electron preferring to reside on the Ti and being repelled by Si still holds. Therefore, a geometric effect is unlikely to be the main cause for the observed difference. But the structural analysis does indicate that the nature of Ti/Zr–O bonding and Si/Ge–O bonding is likely to be different.

A second possible explanation is that the added electron is incorporated into the clusters in different ways. The ionic nature of Ti/Zr–O bonds versus the more covalent nature of Si/Ge–O bonds suggests that the added electron may localize on a Ti(IV) cation in its empty d-shell (as already suggested above) while the extra electron at Si (Ge) would have to be added to an “antibonding” M–O orbital, which would be unfavorable. We test this hypothesis next. Density difference isosurface plots of the added electron carrier at  $x = 1$  in Figure 3a,c,e,g are shown in Figure 4. Each plot is obtained by subtracting the total electron density of the cluster with and without the electron carrier at the geometry optimized with the electron carrier. For Ti (Zr) doping, the electron is added to a Ti (Zr) 3d orbital as expected, based on the ionic nature of the Ti–O (Zr–O) bond. For Si (Ge) doping, the electron density on Si (Ge) delocalizes around three Si–O (Ge–O)  $\sigma$  bonds, corresponding to the three longer Si–O (Ge–O) bonds in Table 3. The lengthening of these bonds and the location of the extra electron provides strong evidence that the extra electron resides in an antibonding Si–O (Ge–O) orbital, as postulated above. Adding the electron to an antibonding orbital is strongly disfavored, which is why the electron greatly prefers to reside on the Fe ion (Figure 3e,g).

Experimentally, Kennedy et al.<sup>17</sup> and Shinar et al.<sup>22</sup> observed greater photoactivity for hematite doped with Si, Ge, Zr, or Hf than when it is doped with Ti. They suggested that Ti<sup>4+</sup> might introduce additional energy levels that trap electrons, while the +3 oxidation states for heavier group IVB elements are unstable,

which we confirmed here. However, Glasscock et al.<sup>21</sup> observed enhanced photoelectrochemical activity with Ti or Si doping with Ti being superior in their experiments. They pointed out that Si doping might be inferior because it produced smaller grains that may increase carrier recombination due to the increased number of grain boundaries. Clearly, differing sample preparation conditions that lead to different microstructures contributes to the observed outcome. Here we are only able to assess the intrinsic mobility at the atomic scale and not the effect of differing microstructures.

We have carried out ab initio electron transfer simulations using an electrostatically embedded cluster model to gain insight into electron transport mechanisms in pure and doped hematite. While it is energetically favorable for an electron carrier to localize on a Ti site at low dopant concentrations, this trapping effect is not observed for Zr, Si, or Ge dopants. The difference between the dopants can be understood by analyzing their relative IPs, the preferred location and density distribution of the added electron carrier, and bond length changes. For n-type doping of hematite, our calculations suggest that Zr, Si, or Ge doping should be greatly preferred over Ti doping for low dopant concentrations and samples with similar microstructures. While all four dopants will improve the carrier density, at low dopant concentrations the electrons will be trapped by Ti but repelled by Zr, Si, or Ge, thereby allowing transport to continue in the latter case via hopping between Fe cations. Although Zr and Si (Ge) doping exhibit similar electron transport energetics, further analysis reveals that they are successful for different reasons. The difference between Ti and Zr originates in their different relative IPs.  $Zr^{3+}$  is more unstable than  $Ti^{3+}$ , and therefore Zr does not trap the electron carrier. The origin of the difference between Ti and Si or Ge lies in the relative ionicity of the metal–oxygen bonds that form. Si and Ge form much more covalent bonds to oxygen and so an added electron would be forced to occupy an antibonding orbital, as evidenced by the dramatic lengthening of Si(Ge)–O bonds. This is highly unfavorable and so the added electron instead greatly prefers to reside on the Fe cations. Thus, doping with Zr/Si/Ge adds carriers but leaves unaffected the mode of transport (i.e., from Fe to Fe), thereby increasing conductivity without decreasing mobility. By contrast, Ti dopants trap electrons, and contribute fewer electron carriers as a result. These findings offer an explanation of the experimental observation of higher photoactivity for Zr, Si, or Ge doping in hematite<sup>17,22</sup> and suggest that Zr-, Si-, or Ge-doped hematite should be pursued further for photoanodes in photoelectrochemical water splitting. More generally, other dopants that form reasonably covalent bonds to oxygen or can be fully ionized so as not to trap carriers (including Ti at high dopant concentrations) should be pursued as well.

## AUTHOR INFORMATION

### Corresponding Author

\*E-mail: eac@princeton.edu.

## ACKNOWLEDGMENT

E.A.C. thanks the U.S. Air Force Office of Scientific Research and the U.S. Department of Energy, Basic Energy Sciences for funding. Research leading to these results also received funding from the European Union Seventh Framework Programme

(FP7/2007-2013) under grant agreement number [254227] to M.C.T. M.C.T. also acknowledges the Sara Lee Schupf Award from the Weizmann Institute and the New-England Foundation stipend from the Technion.

## REFERENCES

- (1) Crabtree, G. W.; Lewis, N. S. *Phys. Today* **2007**, 60 (3), 37.
- (2) Merchant, P.; Collins, R.; Kershaw, R.; Dwight, K.; Wold, A. *J. Solid State Chem.* **1979**, 27 (3), 307–315.
- (3) Bak, T.; Nowotny, J.; Rekas, M.; Sorrell, C. C. *Int. J. Hydrogen Energy* **2002**, 27 (10), 991–1022.
- (4) Hu, Y.-S.; Kleiman-Shwarsctein, A.; Stucky, G. D.; McFarland, E. W. *Chem. Commun.* **2009**, No. 19, 2652–2654.
- (5) Tilley, S. D.; Cornuz, M.; Sivula, K.; Grätzel, M. *Angew. Chem.* **2010**, 122 (36), 6549–6552.
- (6) Marusak, L. A.; Messier, R.; White, W. B. *J. Phys. Chem. Solids* **1980**, 41 (9), 981–984.
- (7) Joly, A. G.; Williams, J. R.; Chambers, S. A.; Xiong, G.; Hess, W. P.; Laman, D. M. *J. Appl. Phys.* **2006**, 99 (5), 053521.
- (8) Cesar, I.; Sivula, K.; Kay, A.; Zboril, R.; Grätzel, M. *J. Phys. Chem. C* **2009**, 113 (2), 772–782.
- (9) Gardner, R. F. G.; Moss, R. L.; Tanner, D. W. *Br. J. Appl. Phys.* **1966**, 17 (1), 55–61.
- (10) Warnes, B. M.; Aplan, F. F.; Simkovich, G. *Solid State Ionics* **1984**, 12, 271–276.
- (11) Kittel, C. *Introduction to Solid State Physics*; John Wiley & Sons, Inc: New York, 2005; p 208.
- (12) Gardner, R. F. G.; Sweett, F.; Tanner, D. W. *J. Phys. Chem. Solids* **1963**, 24 (10), 1183–1186.
- (13) Gharibi, E.; Hbika, A.; Dupre, B.; Gleitzer, C. *Eur. J. Solid State Inorg. Chem.* **1990**, 27 (4), 647–658.
- (14) Mohanty, S.; Ghose, J. *J. Phys. Chem. Solids* **1992**, 53 (1), 81–91.
- (15) Morin, F. *J. Phys. Rev.* **1951**, 83 (5), 1005.
- (16) Kennedy, J. H.; Shinar, R.; Ziegler, J. P. *J. Electrochem. Soc.* **1980**, 127 (10), 2307–2309.
- (17) Kennedy, J. H.; Anderman, M.; Shinar, R. *J. Electrochem. Soc.* **1981**, 128 (11), 2371–2373.
- (18) Cesar, I.; Kay, A.; Gonzalez Martinez, J. A.; Grätzel, M. *J. Am. Chem. Soc.* **2006**, 128 (14), 4582–4583.
- (19) Kumar, P.; Sharma, P.; Shrivastav, R.; Dass, S.; Satsangi, V. R. *Int. J. Hydrogen Energy* **2011**, 36 (4), 2777–2784.
- (20) Kay, A.; Cesar, I.; Grätzel, M. *J. Am. Chem. Soc.* **2006**, 128 (49), 15714–15721.
- (21) Glasscock, J. A.; Barnes, P. R. F.; Plumb, I. C.; Savvides, N. *J. Phys. Chem. C* **2007**, 111 (44), 16477–16488.
- (22) Shinar, R.; Kennedy, J. H. *Sol. Energy Mater.* **1982**, 6 (3), 323–335.
- (23) Sanchez, H. L.; Steinfink, H.; White, H. S. *J. Solid State Chem.* **1982**, 41 (1), 90–96.
- (24) Ishikawa, Y. *J. Phys. Soc. Jpn.* **1958**, 13, 828–837.
- (25) Berry, F. J.; Greaves, C.; Helgason, Ö.; McManus, J.; Palmer, H. M.; Williams, R. T. *J. Solid State Chem.* **2000**, 151 (2), 157–162.
- (26) Zhang, M.; Luo, W.; Li, Z.; Yu, T.; Zou, Z. *Appl. Phys. Lett.* **2010**, 97 (4), 042105.
- (27) Rosso, K. M.; Smith, D. M. A.; Dupuis, M. *J. Chem. Phys.* **2003**, 118 (14), 6455.
- (28) Iordanova, N.; Dupuis, M.; Rosso, K. M. *J. Chem. Phys.* **2005**, 122 (14), 144305.
- (29) Huang, P.; Carter, E. A. *Annu. Rev. Phys. Chem.* **2008**, 59 (1), 261–290.
- (30) Bosman, A. J.; van Daal, H. J. *Adv. Phys.* **1970**, 19 (77), 1.
- (31) Farazdel, A.; Dupuis, M.; Clementi, E.; Aviram, A. *J. Am. Chem. Soc.* **1990**, 112 (11), 4206–4214.
- (32) Domcke, W.; Yarkony, D. R.; Koppel, H. *Conical Intersections: Electronic Structure, Dynamics & Spectroscopy*. World Scientific Publishing Company: New York, 2004.
- (33) Goodenough, J. B. *Prog. Solid State Chem.* **1971**, 5, 145–399.



- (34) Wadt, W. R.; Hay, P. J. *J. Chem. Phys.* **1985**, *82* (1), 284.
- (35) Evjen, H. M. *Phys. Rev.* **1932**, *39* (4), 675–687.
- (36) Finger, L. W.; Hazen, R. M. *J. Appl. Phys.* **1980**, *51* (10), 5362–5367.
- (37) Nakau, T. *J. Phys. Soc. Jpn.* **1960**, *15*, 727–727.
- (38) Benjelloun, D.; Bonnet, J.-P.; Doumerc, J.-P.; Launay, J.-C.; Onillon, M.; Hagenmuller, P. *Mater. Chem. Phys.* **1984**, *10* (6), 503–518.
- (39) Anisimov, V. I.; Zaanen, J.; Andersen, O. K. *Phys. Rev. B* **1991**, *44* (3), 943–954.
- (40) Dudarev, S. L.; Botton, G. A.; Savrasov, S. Y.; Humphreys, C. J.; Sutton, A. P. *Phys. Rev. B* **1998**, *57* (3), 1505–1509.
- (41) Bengone, O.; Alouani, M.; Blochl, P.; Hugel, J. *Phys. Rev. B* **2000**, *62* (24), 16392.
- (42) Perdew, J. P.; Burke, K.; Ernzerhof, M. *Phys. Rev. Lett.* **1996**, *77* (18), 3865–3868.
- (43) Mosey, N. J.; Liao, P.; Carter, E. A. *J. Chem. Phys.* **2008**, *129* (1), 014103.
- (44) Hay, P. J.; Wadt, W. R. *J. Chem. Phys.* **1985**, *82* (1), 299–310.
- (45) Hehre, W. J. *J. Chem. Phys.* **1972**, *56* (5), 2257.
- (46) Bergner, A.; Dolg, M.; Küchle, W.; Stoll, H.; Preuss, H. *Mol. Phys.* **1993**, *80* (6), 1431.
- (47) Francl, M. M. *J. Chem. Phys.* **1982**, *77* (7), 3654.
- (48) Curtiss, L. A.; McGrath, M. P.; Blaudeau, J.-P.; Davis, N. E.; Binning, R. C.; Radom, L. *J. Chem. Phys.* **1995**, *103* (14), 6104.
- (49) Cohen, A. J.; Mori-Sánchez, P.; Yang, W. *Science* **2008**, *321* (5890), 792–794.
- (50) Valiev, M.; Bylaska, E. J.; Govind, N.; Kowalski, K.; Straatsma, T. P.; Van Dam, H. J. J.; Wang, D.; Nieplocha, J.; Apra, E.; Windus, T. L.; de Jong, W. A. *Comput. Phys. Commun.* **2010**, *181* (9), 1477–1489.
- (51) Schmidt, M. W.; Baldridge, K. K.; Boatz, J. A.; Elbert, S. T.; Gordon, M. S.; Jensen, J. H.; Koseki, S.; Matsunaga, N.; Nguyen, K. A.; Su, S.; Windus, T. L.; Dupuis, M.; Montgomery, J. A. *J. Comput. Chem.* **1993**, *14* (11), 1347–1363.
- (52) Morin, F. J. *Phys. Rev.* **1954**, *93* (6), 1195.
- (53) Radtke, G.; Lazar, S.; Botton, G. A. *Phys. Rev. B* **2006**, *74* (15), 155117.
- (54) Droubay, T.; Rosso, K. M.; Heald, S. M.; McCready, D. E.; Wang, C. M.; Chambers, S. A. *Phys. Rev. B* **2007**, *75* (10), 104412.
- (55) Bandyopadhyay, A.; Velez, J.; Butler, W. H.; Sarker, S. K.; Bengone, O. *Phys. Rev. B* **2004**, *69* (17), 174429.
- (56) Velez, J.; Bandyopadhyay, A.; Butler, W. H.; Sarker, S. *Phys. Rev. B* **2005**, *71* (20), 205208.
- (57) Wilson, N. C.; Muscat, J.; Mkhonto, D.; Ngoepe, P. E.; Harrison, N. M. *Phys. Rev. B* **2005**, *71* (7), 075202.
- (58) Huda, M. N.; Walsh, A.; Yan, Y.; Wei, S.-H.; Al-Jassim, M. M. *J. Appl. Phys.* **2010**, *107* (12), 123712.
- (59) Rollmann, G.; Rohrbach, A.; Entel, P.; Hafner, J. *Phys. Rev. B* **2004**, *69* (16), 165107.
- (60) Moore, C. E. *Natl. Stand. Ref. Data Ser. (U. S., Natl. Bur. Stand.)* **1970**, 34.